Journal of Power Sources 196 (2011) 10336–10343

Contents lists available at SciVerse ScienceDirect

Journal of Power Sources

journal homepage: www.elsevier.com/locate/jpowsour

Evaluation of commercial lithium-ion cells based on composite positive electrode for plug-in hybrid electric vehicle applications. Part II. Degradation mechanism under 2 C cycle aging

Matthieu Dubarry[a], Cyril Truchot[a], Bor Yann Liaw[a,*], Kevin Gering[b], Sergiy Sazhin[b], David Jamison[b], Christopher Michelbacher[b]

[a] Hawaii Natural Energy Institute, SOEST, University of Hawaii at Manoa, 1680 East-West Road, POST 109, Honolulu, HI 96822, USA
[b] Energy Storage & Transportation Systems, Idaho National Laboratory, P.O. Box 1625, Idaho Falls, ID 83415-2209, USA

ARTICLE INFO

Article history:
Received 20 June 2011
Received in revised form 18 August 2011
Accepted 18 August 2011
Available online 25 August 2011

Keywords:
Composite cathode
PHEV
Cycle aging
Degradation mechanisms
Loss of lithium inventory
Incremental capacity

ABSTRACT

Degradation phenomena and inference of their underlying mechanisms during 2 C cycle aging in a cell design comprising $\{LiMn_{1/3}Ni_{1/3}Co_{1/3}O_2 + LiMn_2O_4\}$ composite positive electrode are studied and reported in this work. We describe how aging phenomena in the cells were studied and incremental capacity analysis applied to infer cell degradation mechanisms in the cycle aging process. Two stages of degradation were observed in the life cycle under this aging regime. In the first stage, we conclude that loss of lithium inventory was the cause of capacity fade. As a result of such parasitic loss, the cell further suffered from loss of active materials in the second stage, in which the positive electrode kinetics was hampered and the capacity loss accelerated.

1. Introduction

Rechargeable lithium-ion batteries (LIB) are considered viable choices for mobile power and energy storage applications. As more deployments of LIB in advanced powertrain systems are being pursued, uncertainty in confidence with cell performance degradation and life prediction becomes a major impediment in market penetration for plug-in hybrid electric vehicles (PHEV). Understanding cell degradation mechanism specific to PHEV applications is necessary for improving battery performance. Traditionally, cell testing is used to evaluate the battery performance and its aging behavior (as shown in the efforts of the US national laboratories funded by the Department of Energy) in new generations of LIB chemistries [1–7]. However, most of the cell testing is designed to assessing cell performance and degradation, not to analyzing the cell degradation mechanism. Most of analyses on cell degradation are conducted by postmortem characterizations, and most of them are ex situ. The postmortem analysis may reveal the cause of degradation. More than often, the postmortem results cannot be quantitatively correlated to the capacity loss in a cell. In other words, most of the postmortem results are unable to provide temporal resolution and correlation with the underlying mechanism. Furthermore, the analyses are often inconclusive on cause-and-consequence development (due to the lack of temporal correlation), which may lead to the extent of degradation path-dependent. To strive for more clarity on such issues, we recently use the incremental capacity analysis (ICA) technique to derive time-correlated degradation behavior with test conditions to provide better understanding of the battery aging process [7–11].

In our prior work (as explained in Part I) [6,7] we characterized the initial state of a batch of cells and showed that the chosen cells were of high quality with negligible cell-to-cell variations. In this paper (Part II) we focus on the aging behavior of a "nominal sample cell" (NSC) cycled at a 2 C rate. We use electrochemical characterization and analysis techniques [7–11], primarily ICA, to derive temporally resolved information on how cell degrades under the cycle aging conditions. A proper interpretation of ICA results relies on sufficient knowledge of the literature report on the targeted cell chemistry and related information from other characterization results, including postmortem.

The test cells are made by a commercial vendor from composite positive electrode (c-PE) comprising $\{LiMn_{1/3}Ni_{1/3}Co_{1/3}O_2 + LiMn_2O_4\}$ and graphite negative electrode (NE) with conventional electrolyte. Although many prior studies on $\{LiMn_2O_4 + LiMO_2\}$ (M = Co, Ni) c-PE have been reported [12–20], only one, to our knowledge, has reported the

* Corresponding author. Tel.: +1 808 956 2339; fax: +1 808 956 2336.
E-mail address: bliaw@hawaii.edu (B.Y. Liaw).

0378-7753/$ – see front matter © 2011 Elsevier B.V. All rights reserved.
doi:10.1016/j.jpowsour.2011.08.078

initial electrochemical behavior and phase structural changes in the $\{LiMn_{1/3}Ni_{1/3}Co_{1/3}O_2 + LiMn_2O_4\}$ c-PE compositions [21]. The closest study on cycle aging behavior of c-PE is published by Myung et al. [18], in which a cell with graphite || $\{Li_{1.1}Mn_{1.9}O_4 + LiNi_{0.8}Co_{0.15}Al_{0.05}O_2\}$ was cycled for 300 cycles and lost about 4% capacity at 1 C rate. The origin of the capacity loss was not discussed. Cycle aging of $LiMn_2O_4$ (spinel) versus Li [18] and graphite [22–24] have been reported. The capacity loss in the $LiMn_2O_4$ cathode was associated with Mn dissolution and subsequent deposition as MnO_2 on the anode [22]. A postmortem study of a 3 Ah spinel-based commercial cell after cycle aging was reported by Brown et al. [25,26], where they showed a more complicated behavior of degradation in the graphite || $LiMn_2O_4$ system involving loss of active material, loss of lithium inventory and impeding kinetics in both electrodes. The electrochemical behavior of the $LiMn_{1/3}Ni_{1/3}Co_{1/3}O_2$ versus graphite was investigated by Zeng [27] and the capacity loss was reported similar to that of $LiMn_2O_4$, which follows a linear fashion and loses about 5% after 100 cycles at 1 C. The mechanism was attributed to the destruction of the Li-ion migration tunnels. In our study, the cycle aging of the $\{LiMn_{1/3}Ni_{1/3}Co_{1/3}O_2 + LiMn_2O_4\}$ c-PE versus graphite is investigated using a commercial cell. Interpretations of the incremental capacity analysis on the test results are used as the basis to explain the degradation process in a quantitative manner.

2. Experimental

Ten 1.9 Ah 18650 commercial cells were provided by a vendor for evaluation in this report. The cells were surveyed by weight and open circuit voltage (OCV) measurements as received and then subjected to conditioning tests using a Maccor 4300® system. All cells were tested in custom-made battery racks and special attention was made to ensure comparable contact resistance was achieved so the test results would not be altered in any significant manner arbitrarily by external factors.

Following the initial conditioning and characterization, as reported in Part I, the nominal sample cell (NSC) has been chosen and subjected to further evaluation via a simplified reference performance test (RPT) with charge-discharge cycles at C/25, C/5, C/2, 1 C, 2 C, and 5 C to establish its baseline performance characteristics for this chemistry at room temperature. In these constant rate regimes, the cell was discharged and recharged at a specific rate until the cell voltage reached the cutoff condition in the respective regime. The cell was then set for rest for 4 h. The remnant capacity was subsequently measured with an additional C/25 discharge or charge step to the same cutoff condition followed by another 4-h rest. The relaxed cell voltage (RCV) was recorded at the end of each 4-h rest and used for SOC determination. To determine the SOC, we used the method described in Refs. [7–11]. The SOC was inferred by locating the RCV on the pseudo-OCV versus SOC (denoted as *ps*-OCV = *f*(SOC)) curve [7–11]. The *ps*-OCV = *f*(SOC) curve was calculated from averaging the voltages against normalized capacity of the C/25 charge and discharge curves measured from the NSC. The *ps*-OCV = *f*(SOC) curve is rather universal, as validated by several cells within this batch. SOC inferred from the RCV prior to the remnant capacity measurements will be denoted as the end-of-regime (EOR) SOC; thus, SOC for the end-of-discharge (EOD) and end-of-charge (EOC), respectively. SOC inferred from the RCV measured after the remnant capacity measurements will be denoted as the SOC for the beginning-of-charge (BOC) and beginning-of-discharge (BOD), in reference to the SOC at which the next regime will be started accordingly.

Additionally the NSC was tested with an extended voltage range between 4.25 V and 2.4 V, instead of that recommended by the manufacturer (4.2–2.8 V). This protocol was designed with the intent to test the cell beyond the range of operation in order to reveal any potential detriments to cell performance from mild overcharge or overdischarge. The out-of-range voltages could be reached if a string of cells were not properly controlled in a charge or discharge regime. With the extended voltage range imposed in the cycle aging study, we hope to catch these variances in the model and simulation to accurately estimate the extent of charge or discharge.

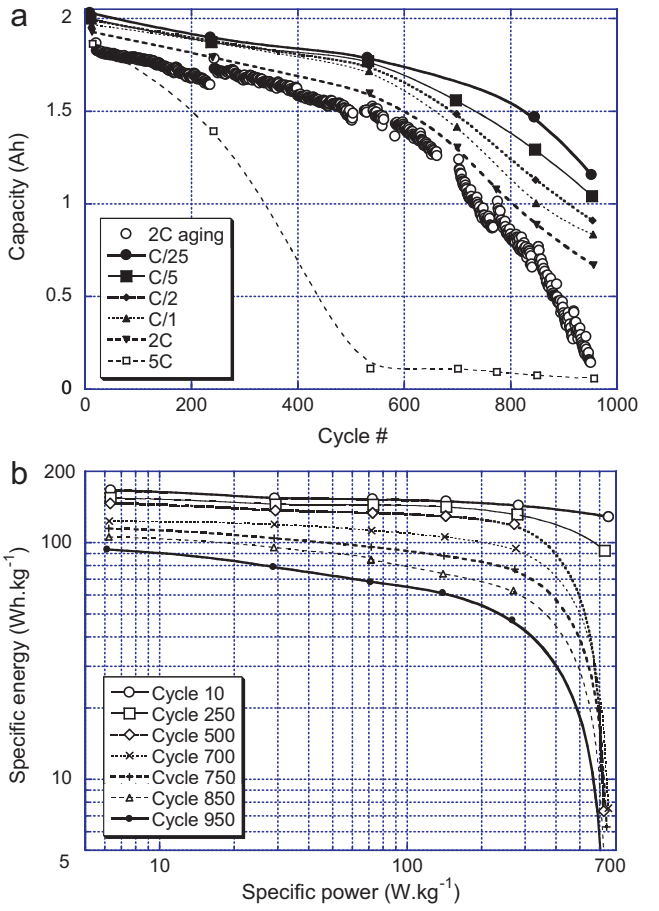

Fig. 1. (a) Capacity variations as a function of cycle number measured during cycle aging and from reference performance tests (RPTs) using different *C*/*n* rates. (b) Ragone plot showing the specific energy and specific power correspondence and its variation with cycle number.

The cell was subsequently subjected to cycling at 2 C rate in the discharge regime while recharging with the protocol typically recommended by the manufacturer with a constant current (CC) step at C/2 followed by a constant voltage (CV) step at 4.2 V with C/25 cutoff at room temperature. The test facility is air-conditioned to maintain a stable temperature. To reduce test duration, the cell was only allowed to rest for 4 h every 10 cycles to trace the SOC changes in the cell. Upon every 10% of capacity loss, the cell was subjected to a RPT to assess changes in performance.

The initial characterization of the cell was presented in Part I [7]. We found that the cells exhibit little cell-to-cell variations. The consistency in the cell quality assures us that the observations of any disparity among the cells in performance do not come from the initial cell-to-cell variations but from test conditions.

3. Results

Fig. 1(a) presents the evolution of capacity changes over the 2 C cycle aging regime (in circles) along with those determined in the RPTs by C/25, C/5, C/2, 1 C, 2 C and 5 C discharges. For rates

below 5 C, the capacity decreases steadily up to about 500 cycles (denoted as the first stage of cycle aging), and the rate capability remains intact. Beyond 500 cycles, the capacity loss accelerates (in the second stage of cycle aging) and the rate capability worsens. During the first stage, the cell loses 0.5 mAh per cycle, which represents 2.5% per 100 cycles. The fade rate is higher than that of the $\{Li_{1.1}Mn_{1.9}O_4 + LiNi_{0.8}Co_{0.15}Al_{0.05}O_2\}$ c-PE (in which 1.33% per 100 cycles was estimated) as reported in Ref. [18]. We should note that the discharge rate in our cycle aging regime (2 C) is higher than the 1 C rate used in Ref. [18]. The fade rate in the targeted chemistry is, nonetheless, only half of those observed in the individual constituents (about 5% per 100 cycles) as reported in Refs. [22,23,27], despite the higher discharge rate used in our cycle aging. In the case of 5 C, the rate capability seems quite limited in this cell chemistry and degrades rapidly in cycle aging; thus, the capacity (denoted as $Q_{0.2}$) is lost completely in the first stage.

In the second stage of cycle aging, rate capability worsens and the fading accelerates (from −1 mAh per cycle at lower rates to −2 mAh per cycle at higher rates). This fading phenomenon resembles the one observed by Ramadass et al. [24] for a commercial graphite || $LiCoO_2$ cell. We should note that the capacities obtained from 2 C cycle aging and from RPTs (particularly the capacity at 2 C) are slightly different because different cutoff voltages were used in the respective tests (i.e. 4.2–2.8 V in cycle aging versus 4.25–2.6 V in RPTs).

USABC test procedures define the end-of-life (EOL) of a battery when it cannot deliver more than 80% of its rated capacity under a specific test protocol. Since the nominal capacity at C/2 (denoted as Q_2) is 1.90 Ah, the EOL is reached when Q_2 falls below 1.52 Ah; thus, the cell reaches its EOL after 650 cycles of aging.

Conventionally, the power capability of a cell should be determined by constant power discharge regimes; thus, it will require performing additional runs of experiments besides the constant current ones. The assessment of power capability could be approximated using the power delivered as derived from the constant current tests by multiplying the average cell voltage with the C/n rate current. This approach provides a reasonable approximation to the constant power tests and the results can represent trade-offs between specific power (SP) and specific energy (SE) for this chemistry in a Ragone plot. Fig. 1(b) presents the evolution of the Ragone plot upon cycle aging. Initially, the cell can deliver 125 Wh kg^{-1} at 650 W kg^{-1}. The SE to meet such a SP requirement decreases noticeably in the aging and becomes less than 10 Wh kg^{-1} after 500 cycles; nonetheless, the cell can still provide 100 Wh kg^{-1} at 200 W kg^{-1} after 700 cycles. The SP evolution upon cycle aging is a reflection of the polarization resistance change in the cell, as $\Delta SP = \Delta(V_{avg}I) = I(\Delta V_{avg}) = I^2\Delta R$ with I being a constant. From this approximation, ΔR was calculated to be about 50 mΩ. The initial internal cell resistance was estimated to be 69 mΩ [6]; thus, the cell resistance might have increased by 70% upon cycle aging.

Fig. 2 displays the evolution of RCVs at the BOD and EOD for several rates over the cycle aging. The initial RCVs in the first three RPTs (or in the first stage of cycle aging) are almost identical for all the rates studied because the cell was allowed to equilibrate up to the BOD. We should also note that, despite a C/25 remnant capacity measurement as the first step in the RPT regime, and with constant current-constant voltage steps in the charge regime that finishes with a C/25 limiting current cutoff in the cycle aging, these BOD RCVs are higher than those measured in the cycle aging regime due to difference in cutoff voltage used in each regime. After the first stage of cycle aging, the BOD RCV begins to decrease gradually, by 50 mV at the end of 950 cycles. The trends of the EOD RCVs are more complicated. In the first stage of cycle aging, the EOD RCVs remain relatively stable for the first 500 cycles (except those of 5 C, which increases quite steadily in this period) and they are rate-dependent. In the second stage of cycle aging, these EOD RCVs begin to increase

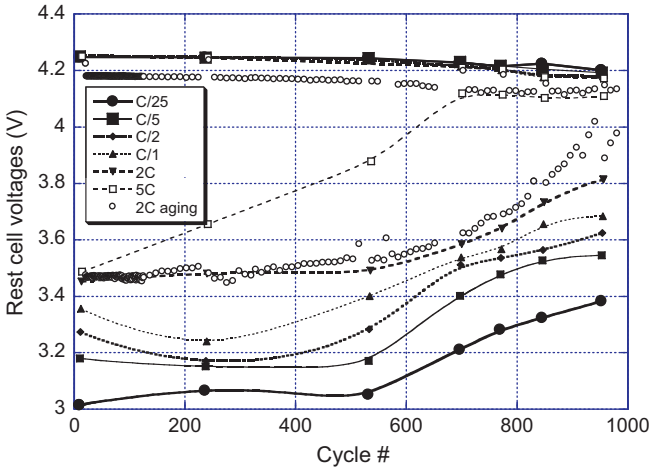

Fig. 2. Rest cell voltages (RCVs) versus cycle number as measured during the cycle aging (in open circles) and from the RPTs at the beginning- and end-of-discharge (BOD and EOD) using different rates.

at considerable paces. These variations with rate and cycle number indicate that the states of the electrodes at the BOD and EOD are varying in a complex manner through cycle aging and need to be investigated further.

4. Discussion

4.1. Incremental capacity variations in the cell

The unique features of the incremental capacity (IC) curve of this $\{LiMn_{1/3}Ni_{1/3}Co_{1/3}O_2 + LiMn_2O_4\}$ c-PE versus graphite NE have been discussed in Part I [7]. Based on the electrode reactions described in the literature [21,28–30], Fig. 3(a) shows the sequence of electrochemical reactions of the c-PE as a function of electrode potential versus a lithium metal reference. Although the polarization effect in this cell might not be the same as those in the reported half-cell experiments, it is safe to assume that the sequence of the electrochemical reactions and the corresponding cell voltage should not be altered in any significant manner from those extracted from the half-cell results in the literature against lithium metal reference. Descending from the high electrode potential, first reacted is the solid solution in $LiMn_{1/3}Ni_{1/3}Co_{1/3}O_2$ (①), which extends from 4.2 V (due to cutoff) to 3.75 V, at which a phase transformation in $LiMn_{1/3}Ni_{1/3}Co_{1/3}O_2$ occurs (④). In this potential range, two phase transformations take place in $LiMn_2O_4$ (② and ③) at 4.1 V and 4.0 V respectively. Overall, the IC signature of the c-PE should resemble the one reported in Ref. [20]. Fig. 3(b) shows the IC peak indexed by convoluting c-PE reactions [17,20] with the five NE reactions, noted as ❶ –❺ . Further details on the IC peak index have been published elsewhere [6,11]. It is important to realize that some of the IC peaks can be used as status indicators for an electrode (or its constituents) [7]. For instance, peak ❶ *② may reflect the state of $LiMn_2O_4$. Vice versa, peaks ❷ *④ and ❺ *④ may exhibit status for $LiMn_{1/3}Ni_{1/3}Co_{1/3}O_2$ and graphite NE, respectively, over cycle aging.

4.2. Stage 1 of cycle aging

Fig. 4 presents the evolution of the IC curves determined by the C/25 discharge regime at cycle 10, 250, and 500. The IC signature of the cell undergoes several evolutions upon cycle aging. The most distinct feature is the evolution of peak intensity associated with peaks ❶ *③ , ❷ *③ , and ❷ *④ with cycle number. The intensity of ❶ *③ and ❷ *④ decreased while that of ❷ *③ increased noticeably with

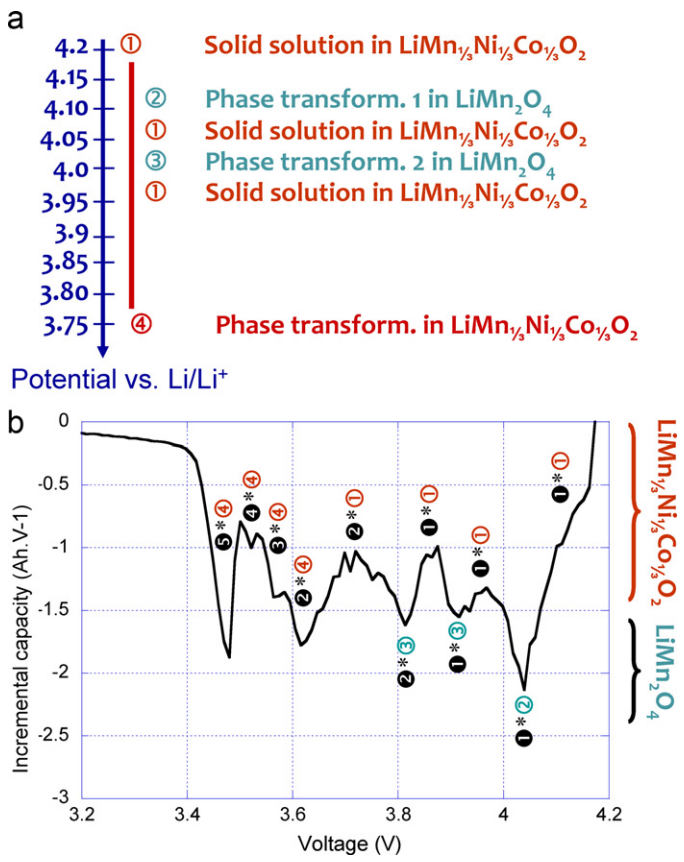

Fig. 3. (a) Schematic illustrates the potential scale of the reactions occur in the composite positive electrode (c-PE) that comprises $\{LiMn_{1/3}Ni_{1/3}Co_{1/3}O_2 + LiMn_2O_4\}$. (b) Convolution and index of the incremental capacity (IC) peaks as a function of cell voltage according to the c-PE reaction against the graphite negative electrode.

possible peak position shifts due to intensity variations. It is difficult to tell if these variations are related to one another or not. In addition, the intensity of peak ❺ *④ seems to decrease slightly between cycle 250 and 500. Despite evolutions in peak intensity, the shape of peaks ❶ *② and ❺ *④ remain almost the same and all peaks return to the same baseline at the cutoff voltage, which indicates that the

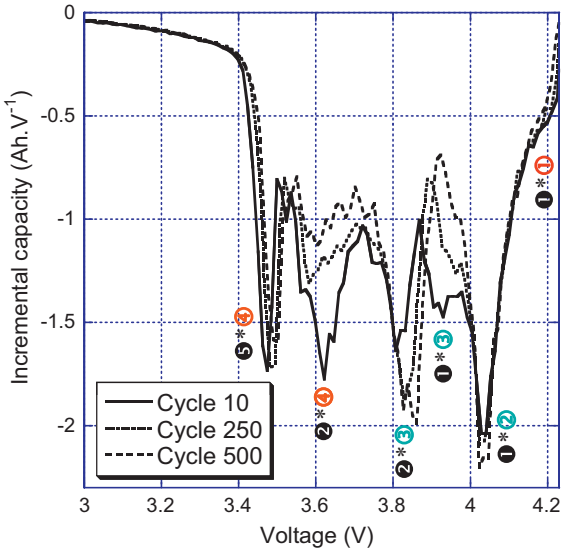

Fig. 4. Evolution of the IC curves in the discharge regime at cycle 10, 250, and 500, representing the change of cell chemistry in the first stage of cycle aging.

kinetics of the cell reaction have not been hampered in any significant manner for c-PE or NE. Therefore, the capacity fade should not be attributed to interfacial kinetics or impedance changes, if any. We should note that peak intensity of ❶ *① might have slightly decreased, indicating that c-PE is less recharged gradually.

The two prominent evolutions in IC peaks are associated with ❶ *③ and ❷ *③, in which ③ is the dominant reaction with $LiMn_2O_4$ in the c-PE. Therefore, the IC peaks separation and the relevant peak intensity changes between the two peaks must come from the NE. A closer look at the intensity changes within these two peaks suggests that the loss in intensity with peak ❶ *③ was made up with the gain in peak ❷ *③ ; in other words, the overall area of peaks (❶ *③ + ❷ *③) remains rather constant. This observation suggests that (1) the amount of active $LiMn_2O_4$ involved in the reaction has not been compromised since full capacity of reaction ③ is retained; (2) the shift in the peak intensity between ❶ *③ and ❷ *③ implies that the extent of Li depletion in the NE have been redistributed from reaction ❶ to ❷ over cycle aging; thus, less and less amount of Li is involved in reaction ❶ through cycling. A plausible explanation of the underlying process is loss of lithium inventory (LLI); thus, Li ions are lost to (yet to-be-identified) parasitic reactions; therefore, less amount of Li return to NE in the charging regime. As a result of LLI, while the full capacity of reaction ③ remains available, the remainder of the capacity that is not engaged in reaction ❶ will then become available for ❷ , leading to an earlier onset and growing ❷ *③ peak intensity. As a cascade effect, the full convolution in ❷ *③ makes the capacity of ❷ available to the convolution with ④ reduced, thus a gradual reduction of ❷ *④ peak intensity through cycle aging. As the cascade effect continues to play out, and the convolution between ❷ and ④ diminishing, the onset for peak ❺ *④ becomes earlier as well with aging. However, the shape of peaks ❶ *② and ❺ *④ remains rather the same, suggesting that the electrode interfacial kinetics are not affected by this cascade effect in capacity fade.

We observed that the intensity of ❶ *① is fairly stable (although it has been diminishing slightly over aging); thus, we suspect that the extraction of Li from the c-PE is not the root of Li loss. We also observed that the overall peak intensity associated with reactions ① , ② , and ③ remain the same, which suggests the associated interfacial kinetics do not impede the capacity release. It is thus fair to say that the amount of c-PE active materials should remain unchanged in this first stage of cycle aging; or, if a loss indeed occurred, it should be quite negligible. We further note that the decreasing intensity in peak ❺ *④ after 250 cycles may imply a possible small loss of active material (LAM) in the NE.

In summary, the linear capacity loss observed for the first 500 cycles is likely associated with LLI at a rate of 0.025% per cycle. We suspect that a minute amount of Li-ions, when leaving the c-PE, was consumed by a parasitic reaction, most likely the formation of the SEI layer on the surface of the NE. It is also interesting to note that we observe either no or probably very insignificant loss of active material on the c-PE, in contrast to the report on the capacity loss in spinel accompanied with the presence of Mn species in the electrolyte solution. Such different observations deserve further attention.

4.3. Stage 2 of cycle aging

During the stage 1 of cycle aging, the RCVs at the EOD are rather stable. This is readily explained by the suggestion that even if c-PE was underused because of LLI, the extent of reaction on the c-PE at the EOD remains on a potential plateau when the Li in the NE is depleted. As reported in Part I, reaction ④ accounts for about 1/3 of the cell capacity [6], around 0.6 Ah. As such, if LLI remains as the only mechanism responsible for the capacity fading, the RCVs should remain the same until the extent of reaction ④ is not being

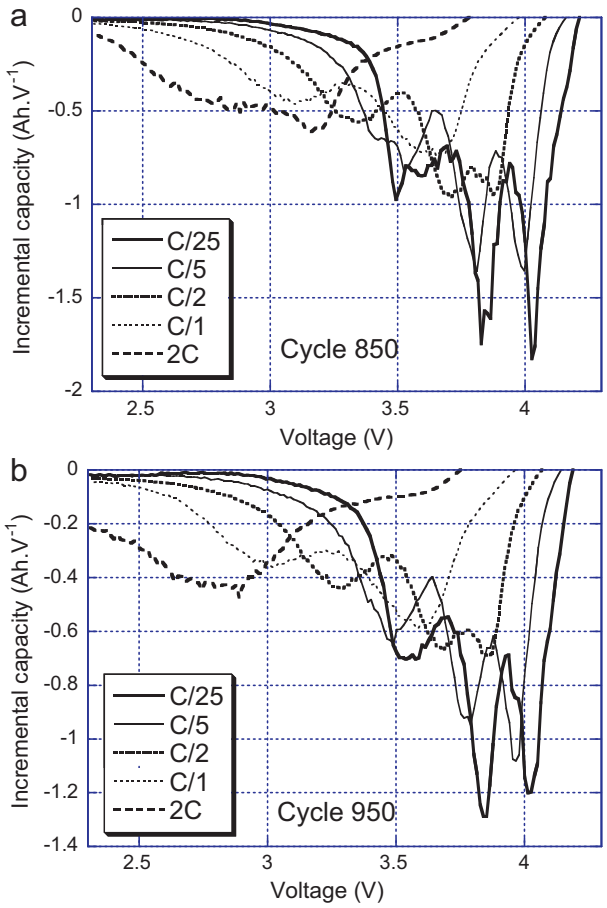

Fig. 5. Evolution of IC curves in the discharge regime at cycle 850 and 950 as a function of *C*/*n* rate to illustrate the rate capability and its impact on cell capacity variations.

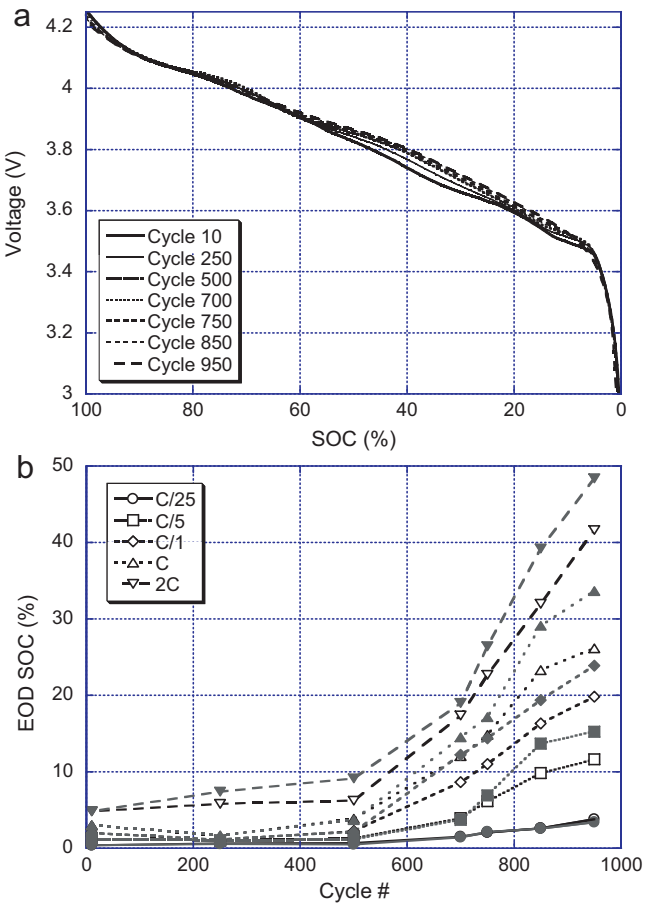

Fig. 6. (a) The *ps*-OCV = *f*(SOC) curves as a function of cycle number. The evolution illustrates the change of cell chemistry through cycle aging. (b) The EOD SOC as a function of cycle number and discharge *C*/*n* rate used in the RPTs. (The open symbols with dark lines are estimated from the evolving *ps*-OCV = *f*(SOC) curves; while the solid symbols with gray lines are inferred from the initial *ps*-OCV = *f*(SOC) curve).

used in the discharge regime. The fact that the RCV starts to increase when only 1/8 of the capacity was released suggests that there must be additional attributes to the capacity loss in the cell degradation.

To search for an explanation to the additional attributes to the capacity loss, we first look into the polarization resistance evolution in the cell through cycle aging. It is quite often reported in the literature that cell polarization resistance could increase with aging and induce premature cutoff in a progressive manner. Fig. 5 presents evidence for this possible explanation using the IC curves at difference rates, from C/25 to 2 C, after 850 and 950 cycles. From the IC curves, the cell polarization resistance was estimated to be 69 mΩ at the BOL and 117 mΩ after 950 cycles. Since the BOD RCV are essentially the same for all rates studied, the relationship between the rate and the initial IR drop (i.e. the onset cell voltage of the first IC peak) is used in the calculation of the resistance using Ohm's law, $\Delta V = R\Delta I$. The increase of 48 mΩ is very close to what we estimated from the change in the Ragone plot, as discussed in Section 3. Over cycle aging, the IC intensity at the EOD cutoff is close to zero for all rates, except 2 C. Since the capacity related to the last reaction has been completely released, despite the polarization resistance increase, the analysis excludes the polarization resistance increase as the main cause to the capacity fading for the EOL. In the case of 2 C, this polarization resistance increase begins to induce under-discharge after 850 cycles. After 950 cycles, the capacity fade come from under-discharge is significant, since the reaction (as inferred by the IC peak) is far from completion at the cutoff.

Since the polarization resistance increase cannot be responsible for the observed capacity fade, a possible attribute to the capacity fade may come from retarded interfacial kinetics, which lead to a decreased extent in the electrode reactions and explain the increase in the EOD RCV. In our previous studies on degradation [7,10] we often infer the RCVs on a *ps*-OCV = *f*(SOC) curve in order to estimate the variation in the EOD SOC and determine the change in the extent of reaction. It is important to point out that in these studies the degradation was induced either by resistance increase in the cell [7] or by LLI on PE that undergoes a single-phase transformation [10]. In both cases, the RCV is not significantly affected by the degradation. In this study, the IC signature from low C rates is significantly altered upon cycling (as shown in Figs. 4 and 5); therefore, we need to be cautious in employing the *ps*-OCV = *f*(SOC) curve (as determined in the initial characterization of the cell), as the cell ages.

To investigate if the *ps*-OCV = *f*(SOC) correspondence remains the same over cycle aging, we compared the EOD SOCs, as inferred from the RCVs and the *ps*-OCV = *f*(SOC) curve, which was determined in the initial RPT or recalculated by averaging the C/25 charge and discharge curves at each of the follow-on RPTs, as exhibited in Fig. 6(a). The evolution of the *ps*-OCV = *f*(SOC) curves over cycle aging shows that the high voltage region (above 3.9 V) and the low voltage region (below 3.4 V) do not seem to vary much by the cycle aging; however, the voltage excursion in the 60–10% SOC range does vary from one to another, especially in the first stage of cycle aging. This observation is a reflection of what has been discussed in Section 4.2. We should note that the low voltage region in the discharge regime corresponds to the Li depletion from the NE and

intercalation in the phase transformation of $LiMn_{1/3}Ni_{1/3}Co_{1/3}O_2$, which occurs on a potential plateau. As a result, the last voltage plateau on the *ps*-OCV = *f*(SOC) curve becomes shorter and its voltage increases with cycle aging. This is consistent with the evolution of the ❺ *④ peak in Figs. 4 and 5. The high voltage region corresponds to the Li intercalation in $LiMn_2O_4$, as depicted by the ❶ *② peak, that is unlikely affected by LLI. Between 3.9 V and 3.5 V, where peaks ❷ *③ and ❷ *④ depict the cell behavior predominantly (Fig. 4), the *ps*-OCV = *f*(SOC) curve is evolving noticeably through cycle aging. This observation is of significance since most of the RCVs in the higher rate regimes rest to this region (see Fig. 2); thus, the EOD SOC inference will be affected substantially.

Fig. 6(b) compares the EOD SOCs as inferred from the progressive *ps*-OCV = *f*(SOC) curves (in dark lines with open markers) to those inferred from the initial *ps*-OCV = *f*(SOC) curve (in gray lines with solid markers). Below 3.4 V the SOCs from the two methods coincide with one another at C/25. For all the other rates, there are significant disparities, sometimes larger than 5%, in the EOD SOCs, depending on the method chosen for the inference.

As described in Section 2, we measured remnant capacity in the cell at the end of each regime. It can be used as a measure to verify SOC as inferred from the RCV using different *ps*-OCV = f(SOC) curves. In order to determine the EOD SOC by the remnant capacity we need to translate the remnant capacity into ΔSOC. This translation could be achieved by using the "capacity ration," as explained in Ref. [6], which is a measure of the amount of capacity associated with 1% SOC for a cell. Since the *ps*-OCV = *f*(SOC) curves evolve through cycle aging, the capacity ration could vary as well. However, in principle, the capacity ration should be rate independent. Thus, it prompts us to conduct the following analysis.

Fig. 7(a) presents the evolution of the capacity ration upon cycle aging based on the ΔSOC as inferred by RCVs from the evolving *ps*-OCV = *f*(SOC) curves and the capacity measured at each given rate. The results are very consistent among all rates. This observation validates the capacity ration is indeed rate independent. The capacity ration varies from 20 mAh %SOC^{-1} at the BOL to 12 mAh %SOC^{-1} after 950 cycles. Since the capacity ration represents the amount of active materials involved in the cell reactions, this evolution therefore suggests that a 40% decrease in the amount of active materials involved in cell reactions upon cycle aging. This decrease follows the same trend with the capacity loss; thus, it is linear for the first 500 cycles (−2%/100 cycles), and then it accelerates in the second stage of cycle aging.

Fig. 7(b) displays the capacity associated with the EOD SOC changes for all rates, as calculated from the combination of evolving *ps*-OCV = *f*(SOC) curve and capacity ration (in black lines with open markers); and those estimated from the initial *ps*-OCV = *f*(SOC) curve and capacity ration (in gray lines with solid markers). It is worth noting that the differences between the two sets of estimation become larger than those shown in Fig. 6(b) towards the EOL, because the decreasing capacity ration amplifies the differences.

Using the remnant capacity (in plain light gray markers without trend line) as a measure for accuracy, we found that the estimate of ΔSOC (and the associated capacity) based on initial *ps*-OCV = *f*(SOC) curve and capacity ration leads to a considerable under-estimation of the remnant capacity. The remnant capacity derived from the evolving *ps*-OCV = *f*(SOC) curve and capacity ration is almost identical to the one measured experimentally. This analysis is of great significance because it validates the approach of using evolving *ps*-OCV = *f*(SOC) curves and capacity rations, which should represent the evolution of the state of the cell chemistry accurately, as one would expect from the thermodynamic perspective.

Fig. 8(a) shows the rate-dependent capacity and its fade based on the evolving *ps*-OCV = *f*(SOC) curve and remnant capacity measured at different rates over the life cycle studied. The capacity and its variation have been normalized in percentage of the initial

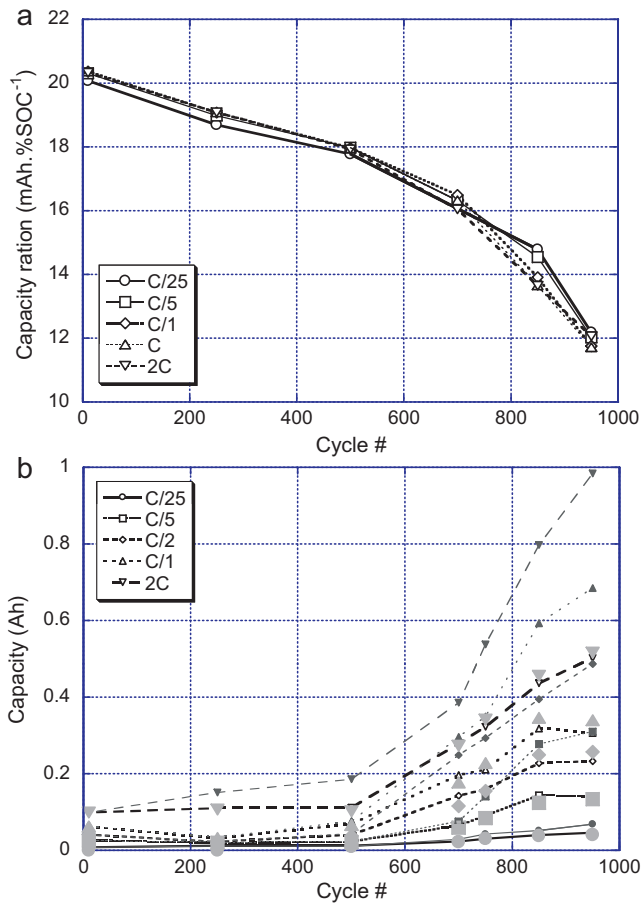

Fig. 7. (a) Capacity ration calculated from the SOC range estimated from the evolving *ps*-OCV = *f*(SOC) curves at different *C*/*n* rates as a function of cycle number. (b) Normalized capacity (versus initial Q_{25}) determined at various *C*/*n* rates in RPTs as a function of cycle number.

maximum capacity (i.e. initial Q_{25}). It is important to point out that the use of evolving *ps*-OCV = *f*(SOC) curve and remnant capacity in the representation of rate-dependent capacity and its changes has precluded the influence of LLI; therefore, this representation of test results is different from that of Fig. 1(a). For the first 500 cycles, as exhibited in the stage one of cycle aging, no detectable hindrance in the cell interfacial kinetics shall induce fade; therefore, the rate-dependent capacities remain rather constant over aging. After 500 cycles, in the second stage of cycle aging, the capacity fade appears, as a result of the kinetic hindrance, and is rate-dependent (as shown in the inset of Fig. 8(a)). The capacity fade increases steadily with aging to 850 cycles before the capacity becoming stabilized. The fade in 2 C remains after 850 cycles. This is a result of under-discharge arisen from the polarization resistance increase, as discussed earlier in the IC analysis, as shown in Fig. 5.

At this juncture, we found the methods to analyze and quantify rate-dependent capacity variation and loss due to LLI and interfacial kinetic hindrance, respectively. We shall then reconcile the contributions from these attributes to account for the total capacity loss exhibited in Fig. 1(a). In the case of C/25, where 42% of capacity loss was measured after 950 cycles, the fade from interfacial kinetic hindrance contributes only 2.5%. The remaining 40% probably come from LLI and other attributes yet to be identified. For 2 C, the 66.6% of capacity loss after 950 cycles comprises about 25% of interfacial kinetic contribution, while the remaining 42% likely are from LLI, under-discharge, and other attributes yet to be identified. Fig. 8(b) shows the discrepancy between those exhibited in Figs. 1(a) and 8(a) for various rates as a function of cycle number.

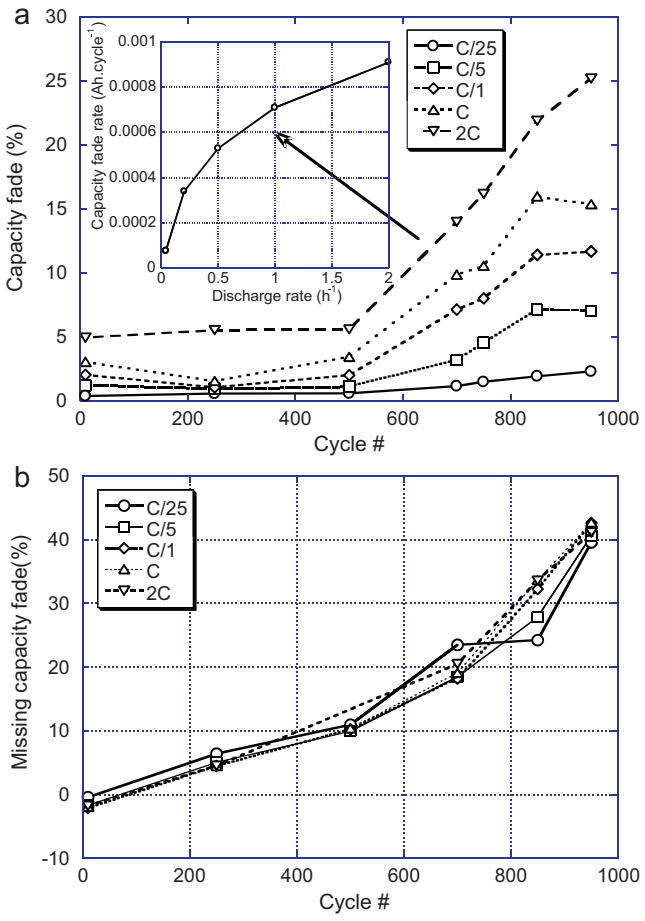

Fig. 8. (a) Capacity fade as a function of cycle number. The inset shows that capacity fade rate as a function of C/n rate. The capacity fade rate is rate-dependent. (b) The discrepancy in capacity fade as a function of cycle number, where the discrepancy was calculated between the total capacity loss as determined in the RPTs through cycle aging and the one estimated from the kinetic hindrance (reduction in the usable SOC range) based on the evolving ps-OCV = f(SOC) curves.

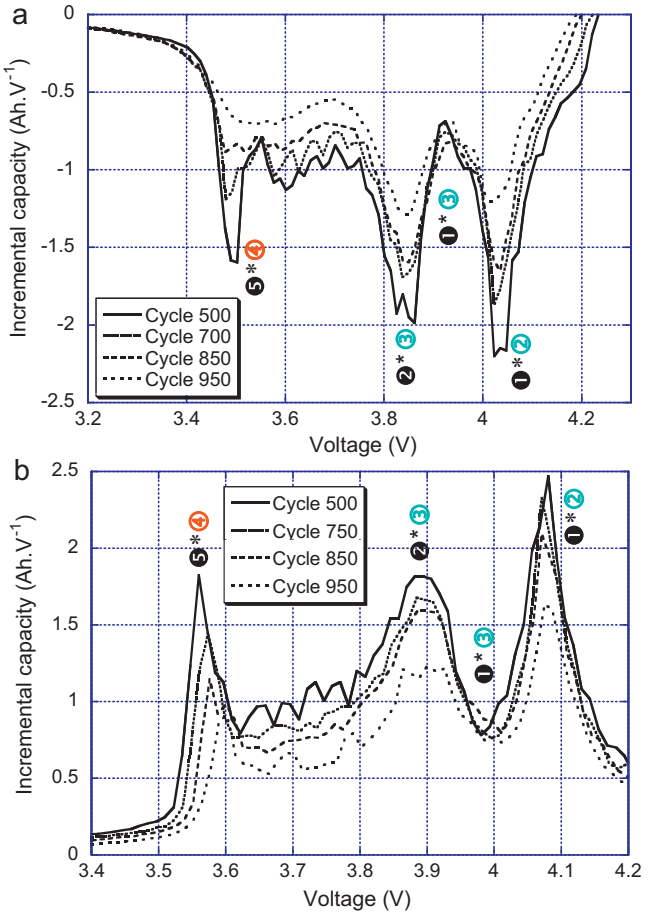

Fig. 9. The IC curves of cycle 500, 700, 850, and 950, in the (a) discharge regime and (b) charge regime, respectively.

It appears that the discrepancy is almost the same for all the rates through cycle aging. The amount of discrepancy as a function of cycle number also agrees with the change in the capacity ration evolution, as shown in Fig. 7(a). This result affirms our assertion that in the first stage of aging, LLI is the predominant attribute responsible for the capacity loss and the evolution of decreasing capacity ration. However, the fade rate of 2% per 100 cycles can account for about 19% of loss after 950 cycles, in contrast to the nearly 40% measured. LLI likely continues throughout the entire cycle aging and rather rate-independent. One could pose a question whether its fade rate increases in the second stage of aging or not. Unfortunately, there is no evidence to suggest a different fade behavior for LLI in the second stage of aging.

Any attribute that can explain the "uncounted for" capacity fade should also contribute to the reduction in capacity ration, which basically represents the amount of active material involved in cell reactions. It is therefore plausible to consider loss of active material as the attribute to the additional capacity fade in the second stage of aging. For instance, it is possible that some grains in the electrodes become isolated from the percolation path and therefore inactive. It is also possible that additional loss of active material is due to dissolution of $LiMn_2O_4$ in c-PE [22], as reported in the literature [25,26].

The incremental capacity analysis of the C/25 charge and discharge curves shall provide some insight, as shown in Fig. 9, where the evolution of the IC curves at cycle 500, 750, 850 and 950 are exhibited. We noted that in charge and discharge regimes, the intensity of peaks ❶ *② and ❷ *③ decrease in a concerted manner. This behavior is uncharacteristic to LLI; for instance, it should not affect these peaks until the capacity of peak ④ is unused entirely. This result is a clear indication that there must be a loss of active material on the c-PE. Since both ❶ *② and ❷ *③ peaks mainly involve reactions on $LiMn_2O_4$, it is evident that loss of spinel is an issue. Moreover, as the shape of both peaks is not altered, the kinetics of the spinel reactions seem intact, suggesting that the material loss might not be kinetic related, yet dissolution of Mn [22] might be an issue.

In the charge regime, the shape of peak ❺ *④ seems intact over cycle aging (Fig. 9(b)); yet, its intensity decreased substantially. It suggests that loss of active material on the NE also incurred. This suggestion is supported by the analysis of the intensity ratio between peaks ❶ *③ and ❷ *③ which remains rather constant, despite continuous LLI. We also noticed that peak ❺ *④ was broadened only during discharge. This behavior could be attributed to retarded kinetics on the NE (❺) or the $LiMn_{1/3}Ni_{1/3}Co_{1/3}O_2$ phase transformation (④). Since it is an asymmetric broadening of peak ❺ *④ between charge and discharge regime, the kinetic hindrance is most likely on $LiMn_{1/3}Ni_{1/3}Co_{1/3}O_2$ (④) [10]. The destruction of the Li-ion migration tunnels has been suggested in Ref. [27], which might explain part of the active material loss. Another plausible cause of loss of active material is a secondary effect of LLI. As LLI continues to grow from the first stage, the SEI formation is a potential source in the production of Li-organophosphates and other polymeric species from the electrolyte decomposition. These side reaction products shall accumulate on the active grain surface,

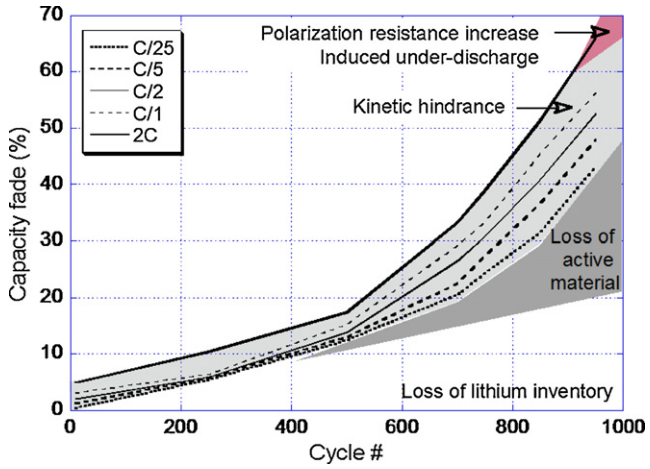

Fig. 10. The capacity fade map under 2 C cycle aging in room temperature depicting the attributes and their contributions to the total capacity fade in the cell as a function of cycle number.

which eventually may cause grain isolation in the electrode matrix; thus, an eventual consequence of loss of active material. Another secondary effect from LLI is the clogging of micropore channels, which limits the mass transport of the reactive Li in the porous electrode. Such phenomenon could show up as sluggish interfacial kinetics due to limited supply of active material in the charge transfer step. Without further (in situ) evidence, we could not be conclusive on deciphering these different underlying mechanisms in the degradation process.

Fig. 10 summarizes the contribution of various attributes to the 2 C capacity fade in the life cycle of this c-PE-based cell chemistry as a function of cycle number, as concluded from the incremental capacity analysis. In the summary figure, the contributions to the capacity fade from kinetic hindrance (polarization and other transport issues) and loss of active material (i.e. LLI and LAM) are all quantitative, as derived from the test data. As the initial fade due to LLI follows a linear relationship in the stage one of the cycle aging, we have no reason to believe that the mechanism and the linear fade would be altered in stage two. Therefore, the fade from LLI should follow the same linear fashion through the course of cycle aging. Without any additional experimental evidence, it is unclear if LLI and LAM are interrelated. The rate-dependent capacity fade from the polarization effect is extrapolated from the cell voltage estimated from the polarization resistance as a function of SOC and rate. By projecting the polarized cell voltage for a given rate to the cutoff, we determine the terminal SOC from the *ps*-OCV = *f*(SOC) curve. From the terminal SOC the capacity and fade are estimated for the given rate as a function of cycle number; thus, leading to the rate-dependent fade rate as shown in the figure.

5. Conclusion

The degradation mechanism of a composite $\{LiMn_{1/3}Ni_{1/3}Co_{1/3}O_2 + LiMn_2O_4\}$-based Li-ion cell was investigated using in situ electrochemical inference approach established by incremental capacity analysis. The results of this study show that the degradation occurs in two stages. In the first stage, the capacity fading seems to come from loss of lithium inventory (LLI). The LLI may occur as a result of parasitic reactions to form SEI layer on the electrode surfaces, although the details of this process remain speculative and need to be investigated further. In parallel, as SEI layer continues to evolve on the surface of the electrodes, it hinders interfacial kinetics and induces loss of active materials in both electrodes in the second stage that accelerates capacity fading. Our results are consistent with those reported in the literature in which losses of positive active material were observed in various occasions. Nevertheless, the inclusion of $LiMn_{1/3}Ni_{1/3}Co_{1/3}O_2$ in the composite positive electrode seems to improve cell performance for more than 500 cycles at 2 C.

More than 80 cells are under testing with different aging protocols to help us understand the degradation mechanisms occurring in the cells and their path dependence. Although additional tests are in progress, the analysis techniques reported in this work shall help us determine the impacts of different duty cycles on the degradation process. We showed that the contribution of LLI, loss of active materials, and kinetic retardation to the capacity fade could be separated and quantified by our inference techniques.

Acknowledgements

The authors gratefully acknowledge funding provided by the Office of Energy Efficiency and Renewable Energy of the United States Department of Energy (Contract No. DE-AC07-05ID14517).

References

[1] R.B. Wright, C.G. Motloch, J.R. Belt, J.P. Christophersen, C.D. Ho, R.A. Richardson, I. Bloom, S.A. Jones, V.S. Battaglia, G.L. Henriksen, T. Unkelhaeuser, D. Ingersoll, H.L. Case, S.A. Rogers, R.A. Sutula, J. Power Sources 110 (2002) 445.
[2] R.G. Jungst, D.H. Doughty, B.Y. Liaw, G. Nagasubramanian, H.L. Case, E.V. Thomas, Proceedings of the 40th Power Sources Conference, Cherry Hill, NJ, June 10–13, 2002.
[3] R.G. Jungst, G. Nagasubramanian, H.L. Case, B.Y. Liaw, A. Urbina, T.L. Paez, D.H. Doughty, J. Power Sources 119/121 (2003) 870.
[4] Idaho National Laboratory, Gen 2 GDR Performance Evaluation Report, INL/EXT-06-11488, Revision 4, July 2006.
[5] I. Bloom, L.K. Walker, J.K. Basco, D.P. Abraham, J.P. Christophersen, C.D. Ho, J. Power Sources 195 (2010) 877.
[6] K.L. Gering, S.V. Sazhin, D.K. Jamison, C.J. Michelbacher, B.Y. Liaw, M. Dubarry, M. Cugnet, J. Power Sources 196 (2011) 3395.
[7] M. Dubarry, C. Truchot, M. Cugnet, B.Y. Liaw, K.L. Gering, S.V. Sazhin, D.K. Jamison, C.J. Michelbacher, Part I, J Power Sources 196 (2011) 10328–10335.
[8] M. Dubarry, V. Svoboda, R. Hwu, B.Y. Liaw, J. Power Sources 165 (2007) 566.
[9] M. Dubarry, V. Svoboda, R. Hwu, B.Y. Liaw, J. Power Sources 174 (2007) 1121.
[10] M. Dubarry, B.Y. Liaw, J. Power Sources 194 (2009) 541.
[11] M. Dubarry, et al., J. Power Sources 196 (2011) 3420.
[12] J.W. Fergus, J. Power Sources 195 (2010) 939.
[13] P. Albertus, J. Christensen, J. Newman, J. Electrochem. Soc. 156 (2009) A606.
[14] B. Scrosati, J. Garche, J. Power Sources 195 (2010) 2419.
[15] Z.F. Ma, X.Q. Yang, X.Z. Liao, X. Sun, J. McBreen, Electrochem. Comm. 3 (2001) 425.
[16] T. Numata, C. Amemiya, T. Kumeuchi, M. Shirakata, M. Yonezawa, J. Power Sources 97 (2001) 358.
[17] H. Kitao, T. Fujihara, K. Takeda, N. Nakanishi, T. Nohma, Electrochem. Solid-State Lett. 8 (2005) A90.
[18] S.-T. Myung, M.H. Cho, H.T. Hong, T.H. Kang, C.-S. Kim, J. Power Sources 146 (2005) 222.
[19] A. Manthiram, W. Choi, Electrochem. Solid-State Lett. 10 (2007) A228.
[20] N.V. Kosova, E.T. Devyatkina, V.V. Kaichev, A.B. Slobodyuk, Solid State Ionics 192 (2011) 284.
[21] K.W. Nam, W.S. Yoon, H. Shin, K. Chung, J. Power Sources 192 (2009) 652.
[22] L. Yunjian, L. Xinhai, G. Huajun, W. Zhixing, H. Qiyang, P. Wenjie, Y. Yong, J. Power Sources 189 (2009) 721.
[23] H.-C. Wu, Z.-Z. Guo, H.-P. Wen, M.-H. Yang, J. Power Sources 146 (2005) 736.
[24] P. Ramadass, B. Haran, R. White, B. Popov, J. Power Sources 111 (2002) 210.
[25] S. Brown, K. Ogawa, Y. Kumeuchi, S. Enomoto, M. Uno, H. Saito, Y. Sone, D. Abraham, G. Lindbergh, J. Power Sources 185 (2008) 1444.
[26] S. Brown, K. Ogawa, Y. Kumeuchi, S. Enomoto, M. Uno, H. Saito, Y. Sone, D. Abraham, G. Lindbergh, J. Power Sources 185 (2008) 1454.
[27] Y.W. Zeng, J. Power Sources 183 (2008) 316.
[28] D. Aurbach, B. Markovsky, I. Weissman, E. Levi, Y. Ein-Eli, Electrochim. Acta 45 (1999) 67.
[29] T. Ohzuku, M. Kitagawa, T. Hirai, J. Electrochem. Soc. 137 (1990) 769.
[30] N. Yabuuchi, T. Ohzuku, J. Power Sources 119/121 (2003) 171.